MAGNETOHYDRODYNAMICS Vol. 59 (2023), No. 3-4, pp. 257–264
DOI: 10.22364/mhd.59.3-4.1

VORTEX PATTERNS OF A MAGNETIC OBSTACLE WAKE

Ji Ryong Cho

College of Engineering, Inje University, 607 Obangdong, Kimhae, 621–749, Republic of Korea
** e-Mail: mechjrc@inje.ac.kr*

The vortex structure of an electrically conducting liquid flowing past a localized magnetic obstacle wake is simulated. When the field strength exceeds a critical value, a localized Lorentz breaking force produces a virtual body filled with a pair of counter-rotating vortices. It is shown that a pair of tail vortices forms behind the body vortex pair to produce a four-vortex pattern if the field strength exceeds a second critical value. Before and after separation of the tail vortex from the body vortex, new vortices of two types emerge between them to produce six-vortex patterns.

Vortices that are produced in electrically conducting liquid flows under the action of external magnetic fields are of considerable fundamental [1–7] and practical [8–11] interest. In this study, we examine the fundamental vortex patterns of a magnetic obstacle wake [12–22]. When a localized magnetic field is applied to the flow of an electrically conducting liquid, the flow deviates laterally because of the Lorentz breaking force. If the field strength is sufficiently large, a stagnation point is produced at which the fluid flow stops. A streamline approaching this point is divided into two separate streamlines that rejoin at a downstream point to form a closed bubble zone called a magnetic obstacle (Fig. 1). Experiments [13], 2D calculations [12], and an analytic approach [14] showed that an inner vortex dipole (called a body vortex here) fills the obstacle body. A combination of numerical simulations and experiments [16] showed that a bifurcation produces a pair of attached vortices (termed tail vortices here) behind the inner vortices when the flow velocity or the field strength increased above a critical value. To satisfy continuity requirements, a connecting vortex pair intervenes between the body and the tail vortex pair. Tail vortices that are pinned to body vortices in the magnetic obstacle wake are geometrically similar to the attached vortices being formed behind bluff bodies [16]. If the flow velocity becomes greater than an instability limit, then the magnetic obstacle wake produces vortex shedding dynamically quasi-similar to the unstable bluff body wakes [15, 17, 18].

The six-vortex body and tail structure of the magnetic obstacle wake described above, composed of body, connecting, and tail vortex pairs, was discovered almost a decade ago, but its uniqueness as a body and tail vortex structure for a magnetic obstacle has not been studied to date. Recent flow visualization experiments [21, 22] indicate that there might be a different body and tail vortex structure. In this work, to answer the question about the uniqueness of this structure, we simulate the formation and bifurcation of the vortex patterns of the magnetic obstacle wake produced by a localized external magnetic field.

Fig. 1 shows a schematic definition of the problem to be considered. An electrically conducting incompressible viscous liquid flows within a rectangular region that is confined by moving side walls, and a localized magnetic field is applied at the centerline. Neglecting possible 3D effects, we follow the 2D approach used by Cuevas *et al.* [14] and Votyakov *et al.* [16].

The non-dimensional Navier–Stokes and induction equations in the quasi-static approximation describe the magnetohydrodynamics as follows:

$$\frac{\partial \mathbf{u}}{\partial t} + (\mathbf{u}\cdot\boldsymbol{\nabla})\,\mathbf{u} = -\nabla p + \frac{1}{\mathrm{Re}}\nabla^2\mathbf{u} + \mathrm{N}\,[\mathbf{j}\times\mathbf{B}]\,, \tag{1}$$

$$\nabla\cdot\mathbf{u} = 0, \quad \mathbf{j} = -\nabla\varphi + \mathbf{u}\times\mathbf{B}, \quad \nabla^2\varphi = \boldsymbol{\nabla}\cdot[\mathbf{u}\times\mathbf{B}]\,, \tag{2}$$

where $\mathbf{u}$ is the velocity field, p is the pressure, $\mathbf{j}$ is the electric current density, and ϕ is the electric potential. In this simulation, the inductionless approximation is employed, as in previous works [14, 16]: $\mathbf{B}$ is the external applied magnetic field, and the internal induced one is not considered. The non-dimensional parameters are the Reynolds number $\mathrm{Re}\equiv u_o L/\nu$ (where u_o is the characteristic velocity, L is the characteristic length, and ν is the kinematic viscosity of the fluid) and the Stuart number $\mathrm{N}\equiv\sigma L B_o^2/\rho u_o$ (where σ is the electric conductivity of the fluid, ρ is the fluid density, and B_o is the magnetic field magnitude). The Reynolds number represents the relative strength of the inertial force with respect to the viscous friction. The Stuart number represents the relative strength of the magnetic breaking Lorentz force with respect to the inertial fluid motion.

The boundary conditions are shown in Fig. 1. For the applied magnetic field, we adopt the following normalized Gaussian distribution [14]:

$$\mathbf{B} = \exp\left(-\beta\left(x^2+y^2\right)\right)\mathbf{e}_z. \tag{3}$$

In the absence of any explicit characteristic length scale L for this problem, Re and N must be set arbitrarily for the simulations. After some preliminary computations, the constant β was set to 5. With this setting, the field strength drops exponentially from 1 at the origin to 1.3×10^{-5} at the nearest point on the wall. This provides sufficient field strength irregularity across the flow channel. This setting results in a magnetic obstacle width $H\approx1$ for $\mathrm{N}\sim10^2$ so that $\mathrm{Re}\sim\mathrm{Re}_H(\equiv u_0 H/\nu)$, which is usually used in the characterization of the vortex pattern in the wake of a solid body [23]. Solid body wakes show instability at $\mathrm{Re}_H > 47$. Analogously, at $\mathrm{N}\sim10^2$, we expect the onset of shear layer instability for a magnetic obstacle at $\mathrm{Re}\sim47$ and the onset of Karman vortex shedding at a somewhat higher Re. The present simulations for $\mathrm{Re}=1\sim100$ and $\mathrm{N}=10\sim10\,000$ should return both stable and unstable wakes, but this work focuses on body and tail vortex patterns of stable wakes.

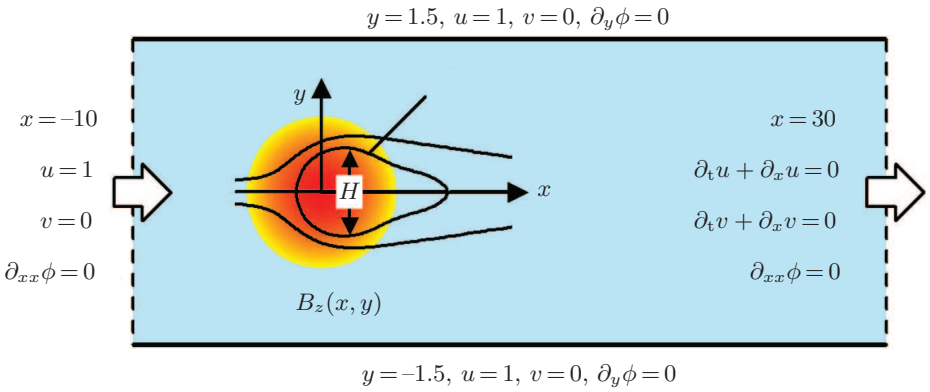

Fig. 1. Schematic presentation of the simulation setup.

Numerical computations were performed using a projection method for incompressible fluid flows [24] that was modified to include the electromagnetic terms and equations. The finite difference method is conservative and shows second-order accuracy in both time and space. The computational grid points, signified by $m_x \times m_y = 221 \times 101$, are clustered around the center of the magnetic field. Fig. 2 illustrates the changes in the flow streamlines with increasing N for $\mathrm{Re} = 65$. The fluid flow inside the channel is retarded under application of the magnetic field because of the Lorenz breaking force, and a lateral flow is induced at $\mathrm{N} = 15$ (Fig. 2*a*). When $\mathrm{N} = 30$ (Fig. 2*b*), the Lorentz breaking force is strong enough to produce a stagnation point close to the center of the magnetic field, and the magnitude of the lateral velocity becomes comparable to that of the streamwise velocity. Streamlines that are divided at the stagnation point rejoin at a downstream point to form a closed bubble zone that we call a magnetic obstacle [16].

The obstacle bodys contour is streamlined because the external flow strains the body in the downstream direction. The formation of a dipole body (DB) vortex pair inside the obstacle body is essential to satisfy the continuity requirement.

When $\mathrm{N} = 45$ (Fig. 2*c*), the increased Lorentz breaking force yields earlier formation of the stagnation point, and also produces a larger obstacle body. However, specific attention is paid here to the shape changes in the streamlines circulating inside the body. The downstream flows inside the body under a strong magnetic field are resisted by the Lorenz force, and the body tends to shrink upwards in these regions. The downstream flows away from the center of the field experience exponentially decaying weak magnetic fields, and the body is strained downwards in these regions because of viscous friction. Additionally, the back flows close to the centerline of the body are deflected in the lateral direction, again because of the Lorentz breaking force. As a result of these actions, the closed streamlines that are nested inside the magnetic obstacle show necking.

The extent of the necking increases with increasing magnetic field strength. When $\mathrm{N} = 150$ (Fig. 2*d*), the necking causes a streamline that is circulating inside the body to cross itself and form a saddle point. As a result, a new tail vortex pair is produced and attached behind the magnetic body vortex pair. These four vortices are nested inside the single obstacle body without violating the continuity of the flow through the saddle point contact. This point attached body and tail (ABT) vortex structure is stable for a wide range of values of both Re and N, as shown below.

When N is almost doubled to 270 from 150, as shown in Fig. 2*g*, we find two separate bubble zones rather than a single bubble. Between these two bubbles, a cavity zone is established. Pairs of counter-rotating vortices are nested inside both the upstream bubble of the magnetic body and the downstream bubble of the tail. This cavity separated body and tail (SBT) vortex pattern is stable because the front surface of the tail experiences the low pressure that develops at the cavity, while the pressure is recovered along the rear tail surface (Fig. 2*h*). As a result, the tail vortex is not carried downwards to follow the external stream. Both the ABT and SBT vortex patterns, which are composed of four vortices in the wake of the magnetic obstacle, were discovered for the first time in this work.

For intermediate values of N between 150, yielding a four-vortex ABT structure, and 270, yielding a four-vortex SBT structure, we observed two vortex patterns that are composed of six vortices. Immediately before the separation of the body and tail vortices that are attached at a saddle point, a parasite vortex is formed between the two vortices (see Fig. 2*e* for $\mathrm{N} = 200$). The backward flows that occur near the centerline between the body and the tail are resisted by the Lorentz breaking force, and these backward flows

are then deflected in the lateral direction. If the local Reynolds number is increased to exceed a critical value, a parasite vortex pair then develops near the centerline in the same way that the magnetic body vortices are formed against the forward mainstream. The flow topology (shown in the inset of Fig. 2*e*) of this point attached body and tail with a parasite (ABTP) vortex structure shows that it is actually a six-vortex structure of Votyakov *et al.* [16]. Immediately after the separation of the tail vortex from the body vortex, a cavity vortex is formed between the two existing vortices (see Fig. 2*f* for N = 210). The external stream that is entrained through the small cavity opening because of the body vortex motion circulates along the bottom boundary of the cavity and

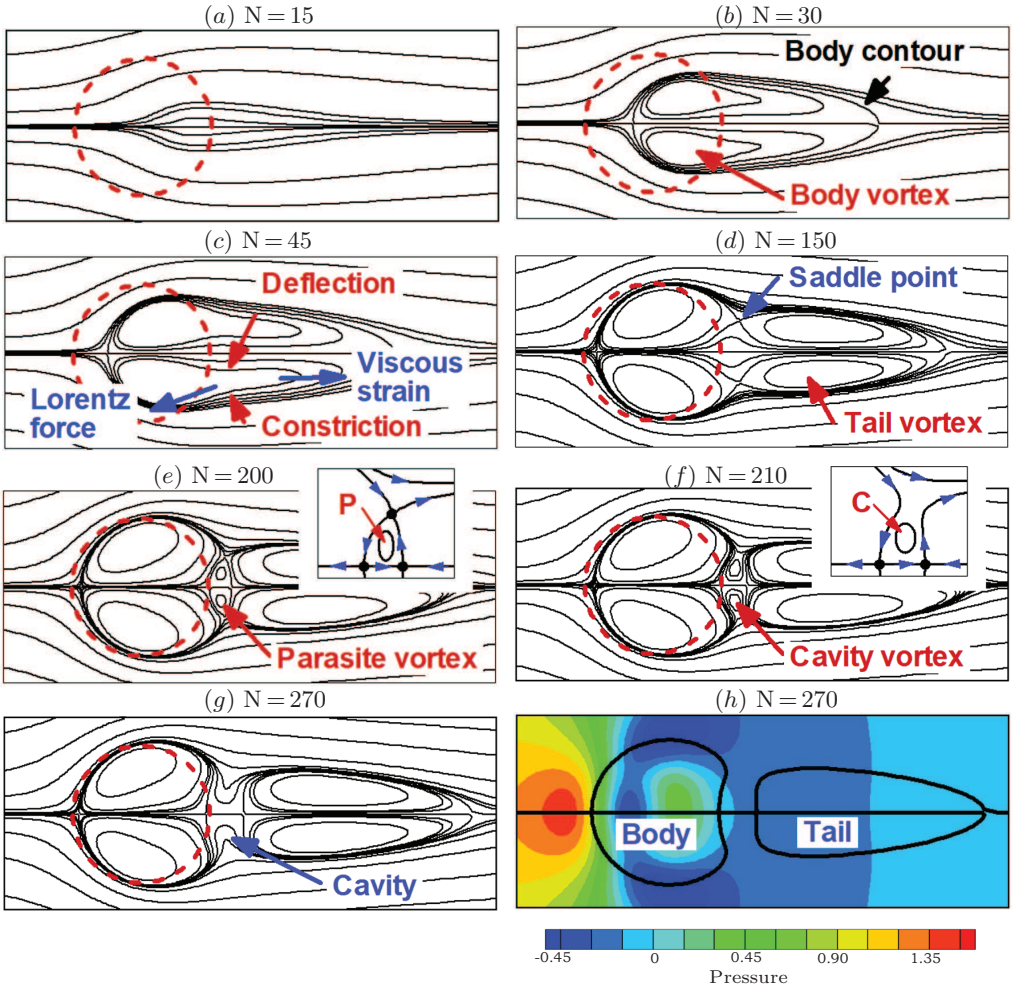

Fig. 2. (*a*)-(*h*) Streamlines and (*h*) pressure field for Re = 65. (*a*) No vortex (NV); (*b*)-(*c*) dipole body (DB) vortices; (*d*) attached body and tail (ABT) vortices; (*e*) ABT with parasite (ABTP) vortices; (*f*) separated body and tail (SBT) vortices with cavity vortices (SBTC); and (*g*) SBT. Dashed circles indicate $r = 0.5$, at which the field strength drops to 0.287 from 1.0 at $r = 0$. The insets in (*e*) and (*f*) represent flow topologies. Small dots indicate the saddle points. The labels P and C denote parasite and cavity vortices, respectively.

draws off through the cavity opening because of the tail vortex motion. This circulation produces a cavity vortex. The flow topology (see the inset of Fig. 2*f*) of this cavity separated body and tail with cavity (SBTC) vortices can be clearly distinguished from that of the ABTP vortex structure. Note that this type of six-vortex structure was observed in recent 3D numerical [20] and experimental [22] studies that were conducted using a rectangular magnet. The SBTC vortex structure was misinterpreted as an ABTP structure in [20], and the flow topology difference between the two vortex structures was not distinguished in [22]. The circulation inside the cavity weakens as the cavity aspect ratio increases with increasing N. Above a specific critical N value, the cavity vortex disappears, and the SBT vortex pattern is produced.

There is also a natural interest in finding vortex structures that occur at remarkably high field strengths and/or remarkably high flow velocities. Fig. 3*a*, where $N = 2000$ and $Re = 26$, shows the emergence of a pair of egg vortices near the center of the magnetic body vortices. If the Lorentz breaking force acting against the backward flows near the centerline is strong enough, a small egg vortex that rotates in the opposite direction to the body vortex appears. The body with an egg vortex (BE) structure was previously observed in a creeping flow (see Fig. 9*b* in [14]). Later, the emergence of a new egg vortex inside the initial egg vortex was found with an increase in the field strength (see Figs. 8*b* and 9*b* in [19]). In principle, we expect an infinite number of egg-inside-egg vortex structures if $N \to \infty$. Fig. 3*b*, where $N = 2000$ and $Re = 40$, shows a cavity separated body and tail with an egg vortex (SBTE) structure. Observation of the emergence of egg vortices inside tail vortices at much higher N values would not be surprising, although this case has not been simulated here. When $Re = 100$ and $N = 200$ (see Fig. 3*c*), unsteady Karman vortex shedding develops in the wake of a localized magnetic field. Under these particular conditions, we can still see the BE vortex pairs, although the symmetry of the

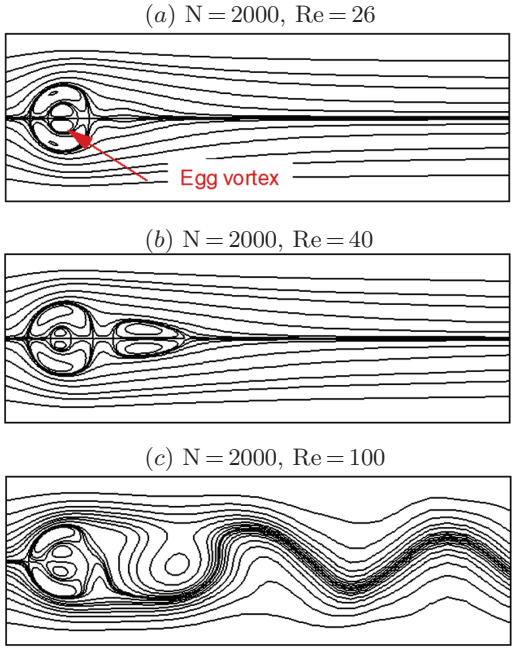

Fig. 3. (*a*) BE vortex pair pattern. (*b*) SBTE vortex pattern. (*c*) Karman vortex (KV) shedding.

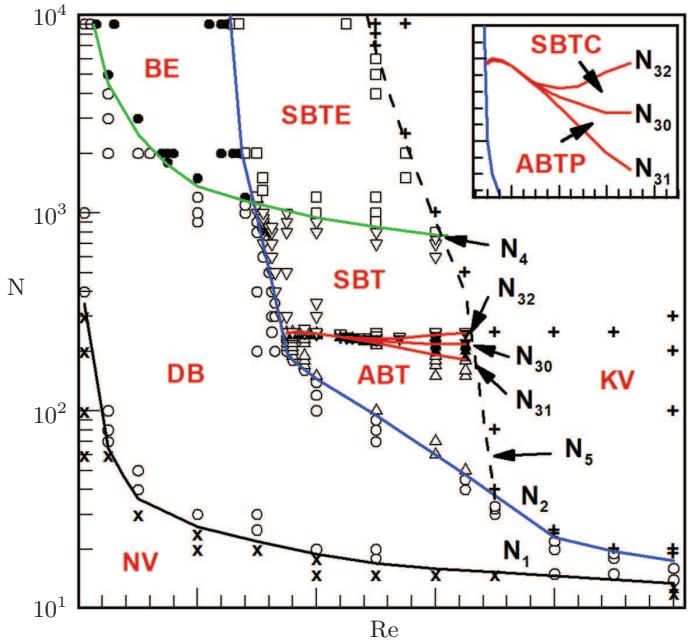

Fig. 4. Bifurcation diagram. Symbols denote vortex patterns: x, NV; ○, DB; ●, BE; △, ABT; ▲, ABTP; ▼, SBTC; ▽, SBT; □, SBTE; and +, KV. The critical lines N_1, N_2, N_{30}, N_{31}, N_{32}, N_4, and N_5 were drawn by eye interpolation.

vortex strength is broken, but we can only see one tail vortex. The tail vortex must, therefore, alternate its rotation direction in accordance with the downstream vortex shedding behavior for flow continuity. Investigation of this unstable vortex pattern in detail is beyond the scope of this study.

Fig. 4 shows a bifurcation diagram. The DB vortex pattern is formed above the first critical magnetic interaction, denoted by $N_1(Re)$. N_1 is approximately 350 at $Re = 1$ but decreases dramatically with increasing Re toward an asymptotic value $N_{1\infty}$ 13. This large variation in N_1 contradicts the previously reported results [16] that were obtained using a rectangular magnet, for which N_1 was almost independent of Re.

Tail vortices attached to the body vortices are produced when $N > N_2(Re)$ and represent a second critical magnetic interaction. The conditions necessary for the formation of stable tail vortices are $Re > 25$ and $N > 36$. The tail vortices are separated from the body vortices but are pinned in space if $N > N_{30}(Re)$, which represents a third critical magnetic interaction. We obtained a four-vortex structure of the ABT vortices pattern for $N < N_{31}(Re)$ and that of the SBT vortices pattern for $N > N_{32}(Re)$. Bifurcation between these two four-vortex patterns occurs directly at $Re < 45$, but it is impossible at $Re > 45$: we obtained an ABTP vortices pattern for $N(N_{31}, N_{30})$ and ab SBTC vortices pattern for $N(N_{30}, N_{32})$. On the bifurcation map, the six-vortex regions that show the ABTP or SBTC vortex patterns are surrounded by four-vortex regions, meaning that direct bifurcation from the DB vortices pattern to the six-vortex patterns is impossible. These findings represent a striking contrast to those of a previous work [16]. In that work, which used a rectangular magnet, a four-vortex pattern was not produced, and the DB vortexs structure bifurcated directly to the ABTP vortexs structure.

The $N_4(Re)$ line indicates a critical magnetic interaction required for the emergence of the egg vortex. The $N_5(Re)$ line indicates a critical magnetic interaction required for the development of unstable Karman vortex shedding. Conversely, the line represents the critical Reynolds number required for Karman vortex shedding, $Re_K(N)$. The magnetic obstacle width H increases with increasing N, and the wake becomes increasingly unstable. Hence, Re_K decreases with increasing N, and $Re_K \to 50$ as $N \to \infty$. The minimum N required for vortex shedding is given as approximately 17.

Now, we are ready to answer the question about the uniqueness of the structure under study: the six-vortex structure of the ABTP vortices pattern that was discovered a decade ago by Votyakov *et al.* [16] is not a unique body and tail vortex structure pattern for a magnetic obstacle wake. We discovered that the tail vortices can be pinned behind the body vortices in two separate ways: by attachment via a saddle point (the ABT vortices pattern), and through separation by a cavity (the SBT vortices pattern). In addition to these two four-vortex patterns, when the cavity width is small, another vortex is produced inside the cavity to yield the six-vortex structure of the SBTC vortices pattern. We also discovered that a vortex dipole cannot reach the six-vortex regions without passing through the four-vortex regions.

Recent experiments of Prinz *et al.* [22] using a rectangular magnet with the same aspect ratio as the magnet of Votyakov *et al.* [16] produced an SBTC vortices pattern rather than an ABTP vortices pattern of Votyakov *et al.* These two patterns represent a subset of the vortex patterns that were discovered in the work described in this paper when using a magnetic point dipole. This means that the vortex patterns of a magnetic obstacle are not solely determined by the external magnetic field profile. The need to find the physical elements that determine the vortex patterns of a magnetic obstacle wake is an issue raised by the study in this paper. The referee commented that the squeezing of flow through a rather narrow space between the magnetic obstacle and the wall could be one possible element changing the vortex pattern bifurcation.

Acknowledgements. This work was supported by grant from Inje University, 2016.

References

[1] D. Rothstein, E. Henry, J.P. Gollub. *Nature*, vol. 401 (1999), p. 770.

[2] G. Hlasz, B. Gyre, I.M. Jnosi, K.G. Szab, T. Tl. *Am. J. Phys.*, vol. 75 (2007), p. 1092.

[3] A. Beltran, E. Ramos, S. Cuevas, M. Brons. *Phy. Rev. E*, vol. 81 (2010), 036309.

[4] D. Krasnov, A. Thess, T. Boeck, Y. Zhao, O. Zikanov. *Phys. Rev. Lett.*, vol. 110 (2013), 084501.

[5] R.C. Cruz–Gmez, L. Zavala-Sansn, M.A. Pinilla. *Exp. Fluids*, vol. 54 (2013), p. 1582.

[6] S. Tympel, T. Boeck, J. Schumacher. *J. Fluid Mech.*, vol. 735 (2013), p. 553.

[7] A. Figueroa, S. Cuevas, E. Ramos. *J. Fluid Mech.*, vol. 815 (2017), p. 415.

[8] H.K. Moffatt. *Phys. Fluids A*, vol. 3 (1991), p. 1337.

[9] A. Thess, E.V. Votyakov, Yu. Kolesnikov. *Phys. Rev. Lett.*, vol. 96 (2006), 164501.

[10] A. Thess, E.V. Votyakov, B. Knaepen, O. Zikanov. *New J. Phys.*, vol. 9 (2007), p. 299.

[11] N. Dubovikova, C. Resagk, C. Karcher, Yu. Kolesnikov. *Meas. Sci. Technol.*, vol. 27 (2016), 055102.

[12] Y.M. Gelfgat, D.E. Peterson, E.V. Shcherbinin. *Magnetohydrodynamics*, vol. 14 (1978), p. 55.

[13] H. Honji, Y. Haraguchi. *J. Phys. Soc. Japan*, vol. 64 (1995), p. 2274.

[14] S. Cuevas, S. Smolentsev, M.A. Abdou. *Phys. Rev. E*, vol. 74 (2006), 056301.

[15] S. Cuevas, S. Smolentsev, M.A. Abdou. *J. Fluid Mech.*, vol. 553 (2006), p. 227.

[16] E.V. Votyakov, Y. Kolesnikov, O. Andreev, E. Zienicke, A. Thess. *Phys. Rev. Lett.*, vol. 98 (2007), 144504.

[17] E.V. Votyakov, E. Zienicke, Y. Kolesnikov. *J. Fluid Mech.*, vol. 610 (2008), p. 131.

[18] E.V. Votyakov, S.C. Kassinos. *Phys. Fluids*, vol. 21 (2009), 097102.

[19] E.V. Votyakov, S.C. Kassinos. *J. Turb.*, vol. 11 (2010), N49.

[20] S. Kenjer, S. ten Cate, C.J. Voesenek. *Int. J. Heat Fluid Flow*, vol. 32 (2011), p. 510.

[21] F. Samsami, Y. Kolesnikov, A. Thess. *J. Visualization*, vol. 17 (2014), p. 245.

[22] S. Prinz, V. Bandaru, Y. Kolesnikov, D. Krasnov, T. Boeck. *Phys. Rev. Fluids*, vol. 1 (2016), 043601.

[23] C.H.K. Williamson. *Ann. Rev. Fluid Mech*, vol. 28 (1996), p. 477.

[24] J.R. Cho. *J. Mech. Sci. Tech.*, vol. 30 (2016), p. 3159.

Received 27.10.2023